The LISA DFACS: Model Predictive Control design for the test mass release phase

Original
The LISA DFACS: Model Predictive Control design for the test mass release phase / Vidano, S.; Novara, C.; Pagone, M.; Grzymisch, J.. - In: ACTA ASTRONAUTICA. - ISSN 0094-5765. - ELETTRONICO. - 193:(2022), pp. 731-743. [10.1016/j.actaastro.2021.12.056]

Publisher:
Elsevier

Published
DOI:10.1016/j.actaastro.2021.12.056

11 October 2021

The LISA DFACS: Model Predictive Control Design for the Test Mass Release Phase[*]

S. Vidano[a]*, C. Novara[a], M. Pagone[a], J. Grzymisch[b]

[a] *Department of Electronics and Telecommunications, Politecnico di Torino, Corso Duca degli Abruzzi 24, 10129 Torino, Italy*

[b] *Guidance, Navigation and Control Section (TEC-SAG), ESTEC, European Space Agency, Kepleralaan 1, Noordwijk 2201 AZ, The Netherlands.*

Abstract

This paper presents a Model Predictive Control (MPC) design for the test mass release phase of the LISA space mission. LISA is a gravitational wave observatory consisting of a triangular constellation of three spacecraft. The gravitational waves are detected by measuring the relative distance between free falling test masses by means of a laser interferometer. Each test mass is a cubic body located inside an electrostatic suspension that is initially locked by a clamp mechanism. Once the plungers are retracted, the test masses are released with high initial offsets and velocities. To detect the gravitational waves, each test mass must be accurately positioned at the cage centre and its attitude must be aligned with the local cage frame. However, the low actuation authority of the electrostatic suspension along with the critical initial conditions, make the attitude and translation control a difficult task. MPC is a suitable technique for this application because it can systematically account for command saturations, state constraints and can provide optimal (or sub-optimal) control inputs by solving an optimization problem online. In this paper, an MPC controller is designed and validated by means of Monte Carlo simulations, achieving satisfactory results.

---

[*] This work is part of the LISA DFACS preliminary prototyping study under the European Space Agency Technology Development Element program.

* Corresponding Author

Email addresses: simone.vidano@polito.it (Simone Vidano), carlo.novara@polito.it (Carlo Novara), jonathan.grzymisch@esa.int (Jonathan Grzymisch)

Keywords: LISA, MPC, GNC, control, spacecraft

Nomenclature

Scalars: $a, b \in \mathbb{R}$.

Column vectors: $\mathbf{r} = (r_1, \dots, r_n) = [r_1 \ \dots \ r_n]^T \in \mathbb{R}^{n \times 1}$

Row vectors: $\mathbf{r}^T = [r_1 \ \dots \ r_n] \in \mathbb{R}^{1 \times n}$

Matrices: $M \in \mathbb{R}^{n \times m}$

Identity matrix: $\boldsymbol{I}_n \in \mathbb{R}^{n \times n}$

Empty matrix: $\mathbf{0}_n \in \mathbb{R}^{n \times n}$

Quaternions: $\mathfrak{q} = (q_0, \mathbf{q}) = \begin{bmatrix} q_0 \\ \mathbf{q} \end{bmatrix}$, $q_0 \in \mathbb{R}$, $\mathbf{q} \in \mathbb{R}^{3 \times 1}$

Quaternion product: $\mathfrak{q} \otimes \mathfrak{p} = (q_0 p_0 - \mathbf{q} \cdot \mathbf{p}) + (q_0 \mathbf{p} + p_0 \mathbf{q} + \mathbf{q} \times \mathbf{p})$

Identity quaternion: $\mathfrak{I} = [1 \quad 0 \quad 0 \quad 0]^T$

Acronyms/Abbreviations

CoM	Center of Mass
CRF	Cage Reference Frame
DFACS	Drag Free and Attitude Control System
DoF	Degree of Freedom
FEM	Finite Element Method
GRS	Gravitational Reference Sensor
IMU	Inertial Measurement Unit
HR	High Resolution mode
LISA	Laser Interferometer Space Antenna
LQR	Linear Quadratic Regulator
MRF	Mass Reference Frame
MPC	Model Predictive Control
MPS	Micro Propulsion System

OA	Optical Assembly
ORF	Optical Reference Frame
PID	Proportional Integral Derivative
RAAN	Right Ascension of the Ascending Node
SC	Spacecraft
SRF	Spacecraft Reference Frame
TM	Test Mass
WR	Wide Range mode

1. Introduction

Gravitational waves are perturbations of the space-time curvature that can be detected by measuring the relative distance between two free falling test masses located at a far distance. Thanks to a quieter environment and the higher distances involved, space-based observatories can have a lower measurement bandwidth than the actual ground-based interferometers [1]. LISA is a constellation of three spacecraft travelling on different inclined heliocentric orbits, whose orbital parameters with respect to a Sun-centred EME2000 frame are reported in Table 1. By changing the coordinates with respect to the ecliptic frame, the orbits in Fig. 1 can be obtained. The upper figure does not have a unitary aspect ratio to better visualize the inclination of the three LISA orbits, while the central figure shows the same orbits with a unitary aspect ratio.

Table 1. LISA orbital parameters with respect to Sun-centred EME2000 frame

	SC1	SC2	SC3
Semi-major axis [km]	149447895.836	149446190.907	149445697.314
Eccentricity	0.0048247	0.0048216	0.0048212
Inclination [deg]	23.9100	23.1394	23.2659
RAAN [deg]	0.1800	0.9537	358.8749
Argument of perihelion [deg]	97.8911	217.3113	339.0441
True anomaly [deg]	262.8702	143.6110	23.6770

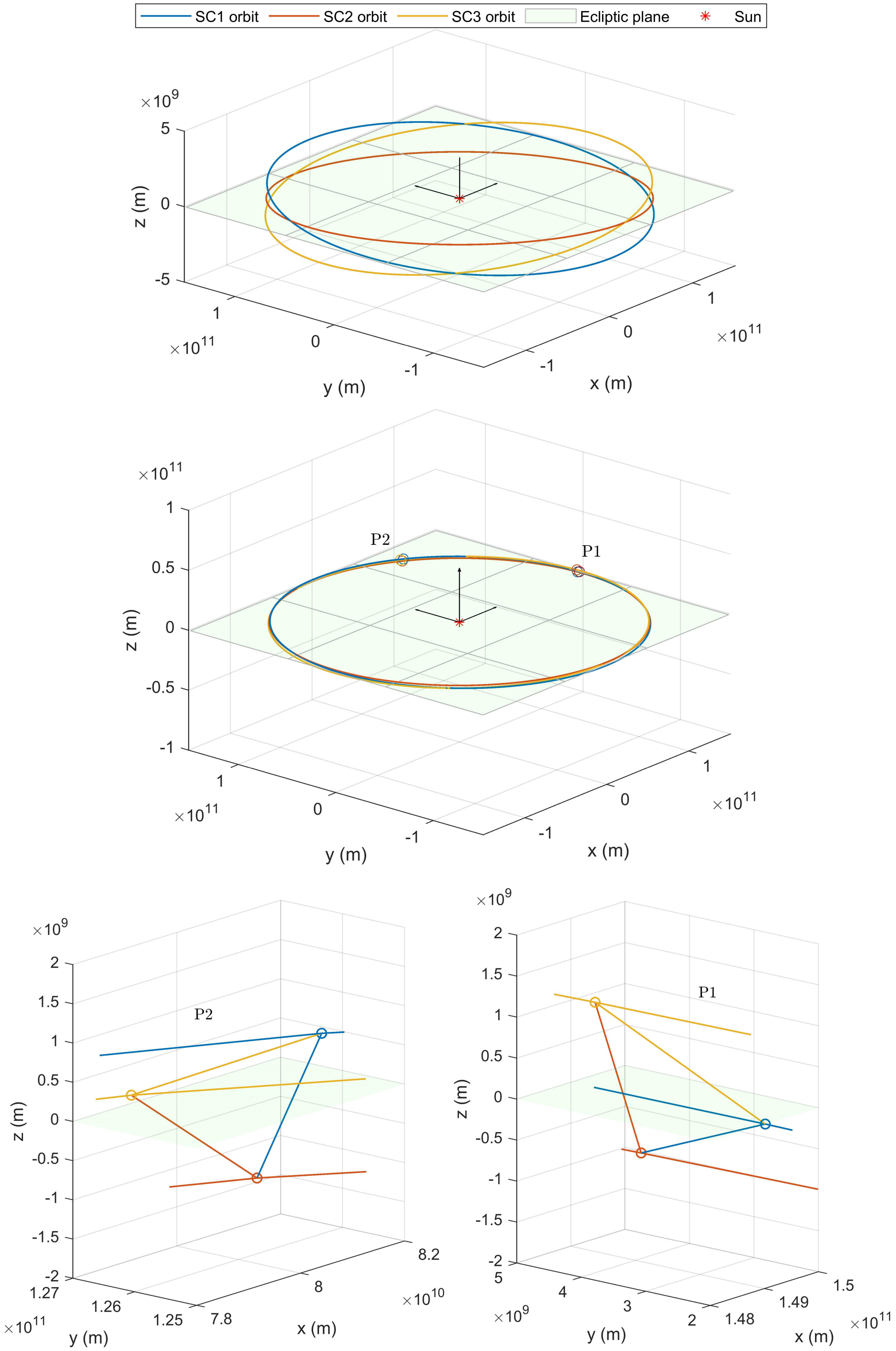

Figure 1 - LISA orbits (top), LISA orbits with unitary aspect ratio (middle), LISA spinning constellation (down)

It can be noted that the LISA orbits are slightly inclined each other and with respect to the ecliptic plane. This particular choice, together with the relative position of the three spacecraft, allows to obtain a Sun-facing spinning triangle with a nominal side length of $2.5 \cdot 10^6$ km. Indeed, the plots at the bottom of Fig. 1 show how the constellation has rotated between the two points highlighted in the central figure.

Gravitational waves are detected by measuring the relative distance between two free falling test masses located on opposite spacecraft. This makes LISA an interferometer with three measurement arms. The spacecraft concept (Fig. 2) consists of a science module that carries two moving Optical Assemblies (OA) whose nominal inter-angle is 60°. Each OA is composed by a telescope, an optical bench for laser interferometry and an electrostatic suspension system (the Gravitational Reference Sensor), which houses a suspended cubic test mass (TM) [2]. A single LISA spacecraft is therefore a multi-body system characterized by 20 degrees of freedom: 6 DoFs for the spacecraft platform, 1 DoF for each optical assembly, 6 DoFs for each test mass.

The mission is divided into 4 main phases: the orbit injection, the test mass release, the constellation acquisition, and the drag free. To withstand the high forces and vibrations at launch, the test masses are initially locked by a clamp mechanism [4]. Once the spacecraft reaches its final orbit, the clamps are retracted, and the test masses are released. To perform science, they must be positioned at the centre of the electrostatic suspension with the same attitude of the local cage frame. However, the low actuation authority along with the critical initial conditions provided by the retraction of the plungers, make the attitude and translation control of the test masses a difficult task. The clamp mechanism was already tested in flight by the technological demonstrator LISA Pathfinder in 2016 [5], obtaining a release performance worse than expected. For instance, the initial roll velocity was 6.8 times worse than the requirement [6]. Due to the high initial velocities, the test masses hit the plungers [6]. After losing part of their kinetic energy, the sliding mode controllers were able to capture the test masses by means of the electrostatic suspensions [6].

In the present work, which is part of the LISA DFACS preliminary prototyping study of the European Space Agency, a Model Predictive Control (MPC) approach is applied to the TM release control problem. MPC applications in the space field are becoming more frequent in the last years [7, 8, 9, 10] thanks to the advantages provided by this control method, such as returning optimal-sub optimal command inputs in presence of saturations and constraints on states. MPC is a suitable technique for this application because (i) it can systematically account for actuator saturations and (ii) it provides optimal (or sub-optimal) control solutions.

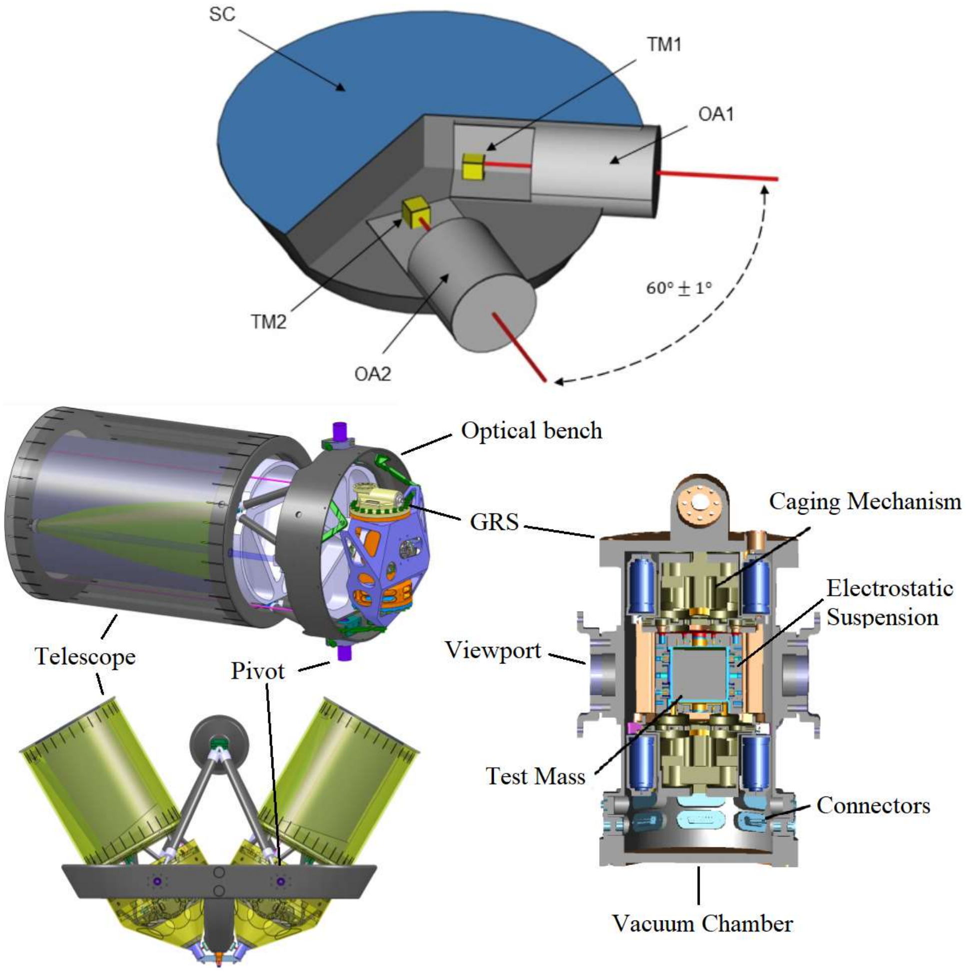

Figure 2 - LISA spacecraft concept [3]

With respect to the sliding mode developed for LISA Pathfinder [6, 11, 12], it is a completely different technique that solves a constrained optimization problem online. In this case, a cost function that depends on the test mass states and the input effort is minimized, while the constraints are the linearized state space model of the system, the input saturations, and the sensing ranges. Moreover, with respect to [6, 11, 12], the present MPC controller is designed to cope with the initial conditions experienced by LISA Pathfinder in-flight and to avoid any collision of the test mass with the surroundings.

With respect to the preliminary MPC presented by the Authors in [13], an extended control architecture, which comprises the spacecraft attitude control loop and the compensation of the solar pressure force, was developed. Moreover, the MPC design was revised improving the performance in terms of transient and steady-state error. The possibility to switch between two different operating modes of the electrostatic suspension system was investigated. Finally, with respect to [13], a Monte Carlo test campaign was carried out.

In the present paper, the plant is briefly described. Then the control architecture, the MPC design and the Monte Carlo results are shown and discussed.

2. Methodology

The MPC [9] solves a constrained optimization problem and finds the optimal or sub-optimal control inputs at every iteration. Furthermore, it requires a prediction model of the plant which is a constraint of the optimization problem. To this purpose, an LTI state space model is usually sufficient. At the first step, an MPC routine initializes the internal predictive model with the last measured/observed states. Then it assigns a preliminary value to the input commands and integrates the predictive model until the prediction horizon. It evaluates the cost function and repeats the previous passages with different input commands until the minimum of the cost function is reached within a certain tolerance. With respect to other classical control methods (i.e., PID, LQR, H-inf and sliding mode), the MPC advantages are that it is a MIMO controller that returns optimal/sub-optimal control inputs by considering saturations on commands and constraints on states. It can minimize the state error and the control action by means of a suitable cost function. Other classical control methods can tackle some of the MPC advantages only partially and not all-together. For instance, LQR can minimize the control effort by means of a suitable cost function, but does not directly involve constraints on inputs and outputs. Same holds for PID and sliding-mode, that can deal with constraints on inputs and outputs only indirectly by means of a suitable tuning of the parameters. In general, the only MPC drawbacks are that the internal prediction model shall be sufficiently accurate to ensure closed loop stability. Moreover, the computational burden could be expensive. In the linear MPC case, this last drawback can be limited by using an explicit MPC form and efficient quadratic programming techniques.

In the present work, an MPC controller is designed for the attitude and translation control of both the test masses after their release, while the spacecraft attitude is controlled by means of a more common state feedback regulator. The nonlinear model of the spacecraft presented in [10] was used to set up a simulation environment in Matlab-Simulink. Then, it was linearized obtaining the internal prediction model for the MPC. The cost function was defined, and the constraints were set according to the characteristics of the actuators and sensors. Finally, the controllers were validated in Monte Carlo simulations.

3. Control Design

3.1 Plant Description

The LISA spacecraft is characterized by 20 degrees of freedom. The six DoFs of the spacecraft platform can be controlled by means of the Micro Propulsion System (MPS), which is a set of 9 cold gas thrusters arranged in three pods on the lateral surface of the spacecraft. The inertial attitude can be determined by means of star trackers. The test mass degrees of freedom can be measured and controlled at the same time by means of an advanced electrostatic suspension called Gravitational Reference Sensor (GRS). The GRS (Fig. 2) is a complex device that contains a 1.96 kg cubic test mass, a vacuum chamber, electrodes, passive mitigation systems for the local disturbances, and the locking mechanism [16]. The whole GRS was tested in-flight by LISA Pathfinder and will be inherited by LISA. Two operating modes are foreseen, the Wide-Range mode involves higher voltages and consequently higher saturations ($\bar{u} \approx 1$ μN) and noises. On the contrary, the High-Resolution mode provides only few nN of actuation authority but introduces lower noises in the loop. Further details about saturations, sensing ranges and noises are reported in the Appendix. To cope with the initial conditions experienced by LISA Pathfinder, the Wide Range mode must be initially used to capture the test mass, then a transition to High Resolution mode could be performed at steady state to reduce the actuation and sensing noises.

According to [5, 17], adhesion phenomena and force asymmetries during the plunger retraction provided to the test mass some initial conditions that were higher than expected in-flight. According to [6], the highest initial conditions occurred on the lateral translation coordinate (-454.6 μm, -22.3 μm/s) and on the roll coordinate (15.4 mrad, 687 μrad/s). These relatively high initial offsets and velocities, together with the low actuation authority of the GRS, make difficult the test mass capture.

One last characteristic of the plant that affects the control is given by the so-called TM stiffness. According to [18], the interactions of the test-mass with the spacecraft gravitational and electromagnetic fields determine the presence of couplings (stiffness) between TM and SC. Due to these couplings, any relative position and attitude jitter between TM and SC is the source of a direct acceleration disturbance acting on the TM. According to [18], this acceleration disturbance can be modelled as a linear combination of position and attitude displacements of the test-mass relative to the cage frame. This model, is also considered by [19, 20] and is reported in Eq. (1)

$$\begin{bmatrix} F_{Sx} \\ F_{Sy} \\ F_{Sz} \\ M_{Sx} \\ M_{Sy} \\ M_{Sz} \end{bmatrix} = K_S \begin{bmatrix} \delta_x \\ \delta_y \\ \delta_z \\ \delta_\varphi \\ \delta_\theta \\ \delta_\psi \end{bmatrix} = \begin{bmatrix} k_{xx} & k_{xy} & k_{xz} & k_{x\varphi} & k_{x\theta} & k_{x\psi} \\ k_{yx} & k_{yy} & k_{yx} & k_{y\varphi} & k_{y\theta} & k_{y\psi} \\ k_{zx} & k_{zy} & k_{zz} & k_{z\varphi} & k_{z\theta} & k_{z\psi} \\ k_{\varphi x} & k_{\varphi y} & k_{\varphi z} & k_{\varphi\varphi} & k_{\varphi\theta} & k_{\varphi\psi} \\ k_{\theta x} & k_{\theta y} & k_{\theta z} & k_{\theta\varphi} & k_{\theta\theta} & k_{\theta\psi} \\ k_{\psi x} & k_{\psi y} & k_{\psi z} & k_{\psi\varphi} & k_{\psi\theta} & k_{\psi\psi} \end{bmatrix} \begin{bmatrix} \delta_x \\ \delta_y \\ \delta_z \\ \delta_\varphi \\ \delta_\theta \\ \delta_\psi \end{bmatrix} \tag{1}$$

where $\boldsymbol{F}_S = [F_{Sx} \quad F_{Sy} \quad F_{Sz}]'$, $\boldsymbol{M}_S = [M_{Sx} \quad M_{Sy} \quad M_{Sz}]'$ are the stiffness force and torque disturbance, K_S is the stiffness matrix containing the stiffness coefficients, $\delta_r = [\delta_x \quad \delta_y \quad \delta_z]'$, $\delta_\vartheta = [\delta_\varphi \quad \delta_\theta \quad \delta_\psi]'$ are the test-mass position and attitude displacements relative to the cage frame. Eq. (1) can be considered as a system of virtual springs and the main consequence is that it generates cross couplings between all the degrees of freedom of the test mass. For instance, a vertical displacement δ_z determines disturbance acceleration components on all the other coordinates, which in turn determine other test-mass displacements giving rise to an unstable behaviour. Possible values of K_S are shown in [19] where they have been obtained by means of a FEM model of the LISA spacecraft. In [20], the online estimation algorithm that was used during the precursor mission LISA Pathfinder is discussed. In particular, an on-board identification experiment was carried out, where some test input-signals have been applied to the test-mass by means of the electrostatic suspension. Then, the stored data were transmitted to Earth and the stiffness parameters have been identified by means of an instrumental variables method. A similar approach could be also repeated in LISA for the estimation of the parameters based on real measurements. In the present work, a K_S matrix obtained in recent LISA Phase-A studies was assumed, given by

$$K_S = \begin{bmatrix} 5 \cdot 10^{-7} & 6 \cdot 10^{-8} & 6 \cdot 10^{-8} & 4.6 \cdot 10^{-1} & 4.6 \cdot 10^{-1} & 1 \cdot 10^{-9} \\ 6 \cdot 10^{-8} & 2 \cdot 10^{-6} & 6 \cdot 10^{-8} & 4.6 \cdot 10^{-10} & 4.6 \cdot 10^{-1} & 4.6 \cdot 10^{-1} \\ 6 \cdot 10^{-8} & 6 \cdot 10^{-8} & 2 \cdot 10^{-6} & 1 \cdot 10^{-9} & 4.6 \cdot 10^{-10} & 4.6 \cdot 10^{-10} \\ 1.1 \cdot 10^{-6} & 1.1 \cdot 10^{-6} & 2.2 \cdot 10^{-6} & 2 \cdot 10^{-6} & 6 \cdot 10^{-8} & 6 \cdot 10^{-8} \\ 1.1 \cdot 10^{-6} & 1.1 \cdot 10^{-6} & 1.1 \cdot 10^{-6} & 6 \cdot 10^{-8} & 1 \cdot 10^{-6} & 6 \cdot 10^{-8} \\ 2.2 \cdot 10^{-6} & 1.1 \cdot 10^{-6} & 1.1 \cdot 10^{-6} & 6 \cdot 10^{-8} & 6 \cdot 10^{-8} & 1 \cdot 10^{-6} \end{bmatrix}. \tag{2}$$

By considering position displacements δ_r in the order of 10^{-3} m, attitude displacements δ_ϑ in order of 10^{-3} rad and the coefficients in Eq. (2), the stiffness forces and torques can reach values in the order of 10^{-9} N and 10^{-9} Nm, that are comparable with the control authority of the electrostatic suspension.

3.2 Reference Frames

For the test mass release phase, the following reference frames are defined (Fig. 3):

- Inertial Frame (IRF): centered in the Sun;
- Spacecraft Frame (SRF): centered in the spacecraft CoM, the z-axis comes out from the upper solar panel, while the x-axis is the bisector of the angle between the optical assemblies;
- the Cage Frame (ORF): centred on the cage centre of the GRS, the x-axis is parallel to the telescope symmetry axis and the z-axis is parallel to that one of the spacecraft frame ($o_{31} \parallel o_{32} \parallel s_3$);

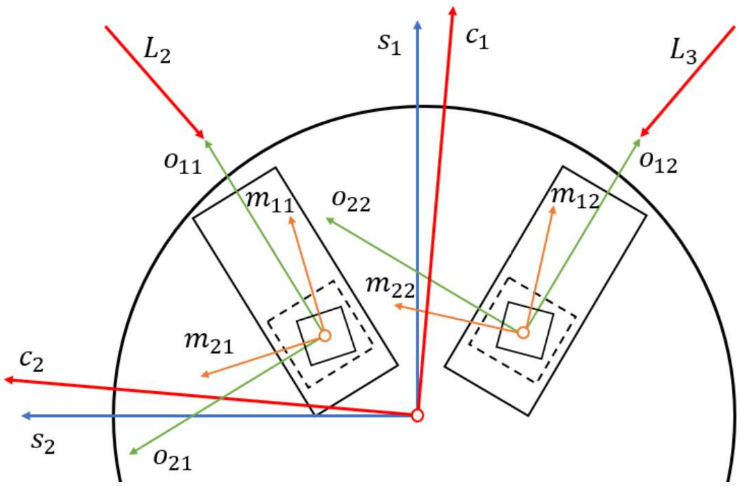

Figure 3 - LISA reference systems

- the Mass Frame (MRF): centred on the test mass CoM and the axes are perpendicular to the cube's faces.

3.3 Control Architecture

During the release phase is fundamental to:

- *Control the test mass attitude and position*.

  The test mass must be positioned at the cage center with a small residual velocity and with an attitude aligned with the cage reference frame. During the release, it must be avoided to hit the inner walls of the electrostatic suspension or the plungers.

- *Control the spacecraft attitude.*

  Keep the reference attitude provided by Ground and compensate for any disturbance torque (i.e. solar pressure torque).

- *Compensate the solar radiation pressure force.*

  The solar radiation pressure must be compensated both to avoid that the spacecraft is being pushed away from the expected orbit and to avoid that the origin of the cage frame translates and escapes from the test-mass. This can be better visualized in the scheme in Fig. 4, where the blue box is the spacecraft, the black box is the GRS cage, the orange box is the test-mass and the green arrows are the cage frame. Before the release, the test-mass is fixed to the spacecraft and the two bodies have the same acceleration (a). After the release, the test-mass has some non-zero initial conditions provided by the retraction of the clamps. Moreover, the spacecraft and the test mass are two separated bodies (even though one is suspended inside the other). In this situation, the solar radiation pressure $\boldsymbol{d}_{srp}$ is acting only on the external surface of the spacecraft and not on the test mass, meaning that the spacecraft will translate subject to $\boldsymbol{d}_{srp}$ and will start to move relative to the test-mass.

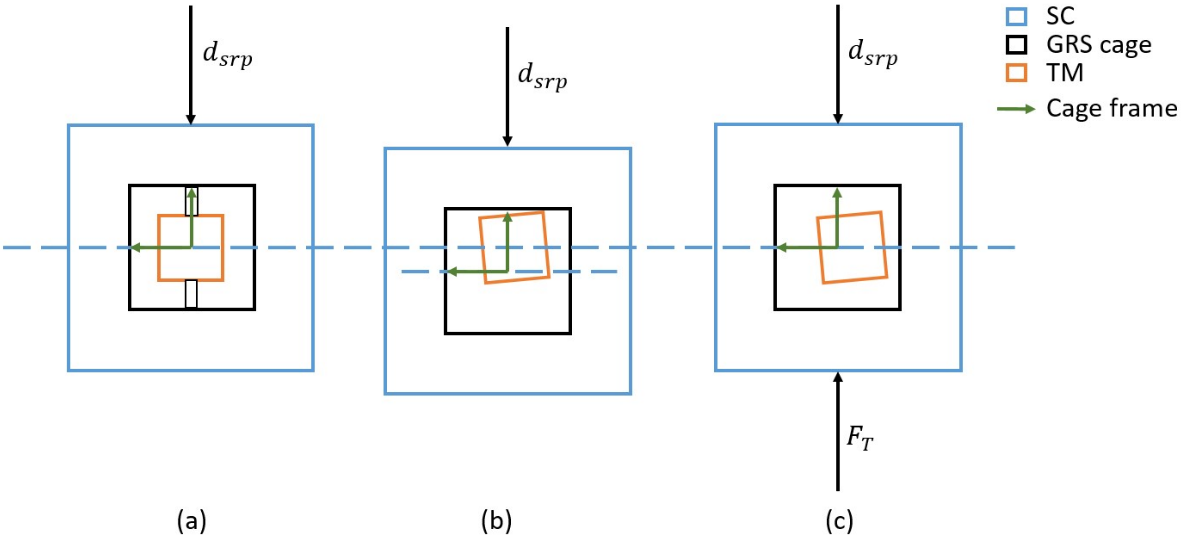

Figure 4 – Effects of solar radiation pressure during TM release

This means also that the origin of the cage frame translates, while in the meantime the test-mass is trying to reach this reference point due to the electrostatic control (b). To avoid this undesirable "escape & follow" situation, the solar radiation pressure force should be compensated by means of the cold-gas thrusters that generate the force $\boldsymbol{F}_T$ (c). In this way, the cage frame origin does not translate anymore and this facilitates the test-mass capture. Furthermore, another effect of the $\boldsymbol{d}_{srp}$ compensation is that the spacecraft is not subject to an orbit drift.

- *Prepare the system to enter drag free mode.*

  The transition from Wide Range to High Resolution mode shall be performed to reduce the noises in the loop.

To achieve these goals, the inertial quaternion of the spacecraft $\mathbf{q}_{SI}$ is measured by the star trackers and controlled by the MPS. The position of the test mass relative to the cage centre $\boldsymbol{r}_M$ and the test mass attitude relative to the cage reference frame $\boldsymbol{\vartheta}_M$ are controlled and measured by the GRS. The control loops are (see Fig. 5):

- *Closed loop spacecraft attitude control.*

  The inputs of controller K_{SC} are the reference quaternion $\boldsymbol{\mathfrak{q}}_r$ provided by Ground and the estimated state vector $\hat{\boldsymbol{x}}_{SC} = (\hat{\boldsymbol{\mathfrak{q}}}_{SI}, \hat{\boldsymbol{\omega}}_{SI})$. The control command is the torque $\boldsymbol{M}_T$ generated by the MPS. The control goal is to regulate the error quaternion such that $\boldsymbol{\mathfrak{q}}_e = \boldsymbol{\mathfrak{q}}_{SI}^{-1} \otimes \boldsymbol{\mathfrak{q}}_r \rightarrow \boldsymbol{\mathfrak{I}}$. A simple state feedback regulator was considered for the control design.

- *Closed loop test mass attitude and translation control.*

  The inputs of the i-th controller K_{TM} are the reference vector $\boldsymbol{y}_{\mathrm{r}} = \boldsymbol{0}$, since we want to reach the cage centre with an attitude equal to the cage reference frame, and the estimated state vector $\hat{\boldsymbol{x}}_{Mi} = (\hat{\boldsymbol{r}}_{Mi}, \hat{\boldsymbol{v}}_{Mi}, \hat{\boldsymbol{\vartheta}}_{Mi}, \hat{\boldsymbol{\omega}}_{Mi})$, which is needed to initialize the internal prediction model of the MPC. The control commands are the electrostatic forces an torques of the GRS $\boldsymbol{F}_E$, $\boldsymbol{M}_E$.

- *Open loop compensation of the solar pressure force.*

  The inertial position of the satellite is not measured/observed, no IMU accelerometers are foreseen for now and the GRS cannot be used as an accelerometer since the test mass is still being controlled by the electrostatic suspension, in order to be placed at the centre of the cage and aligned with the cage frame. Therefore, the controller K_{SP} is an open loop physical model that exploits the attitude quaternion of the spacecraft $\hat{\boldsymbol{\mathfrak{q}}}_{SI}$ to compute the solar pressure components in the spacecraft reference frame. The control commands $\boldsymbol{F}_T$ will have the same modulus of the solar pressure force, but with opposite sign.

Preliminary attempts of designing a unique MPC controller for the whole plant were not successful, due to the tuning/scaling difficulties and the higher computational load of the optimization algorithm.

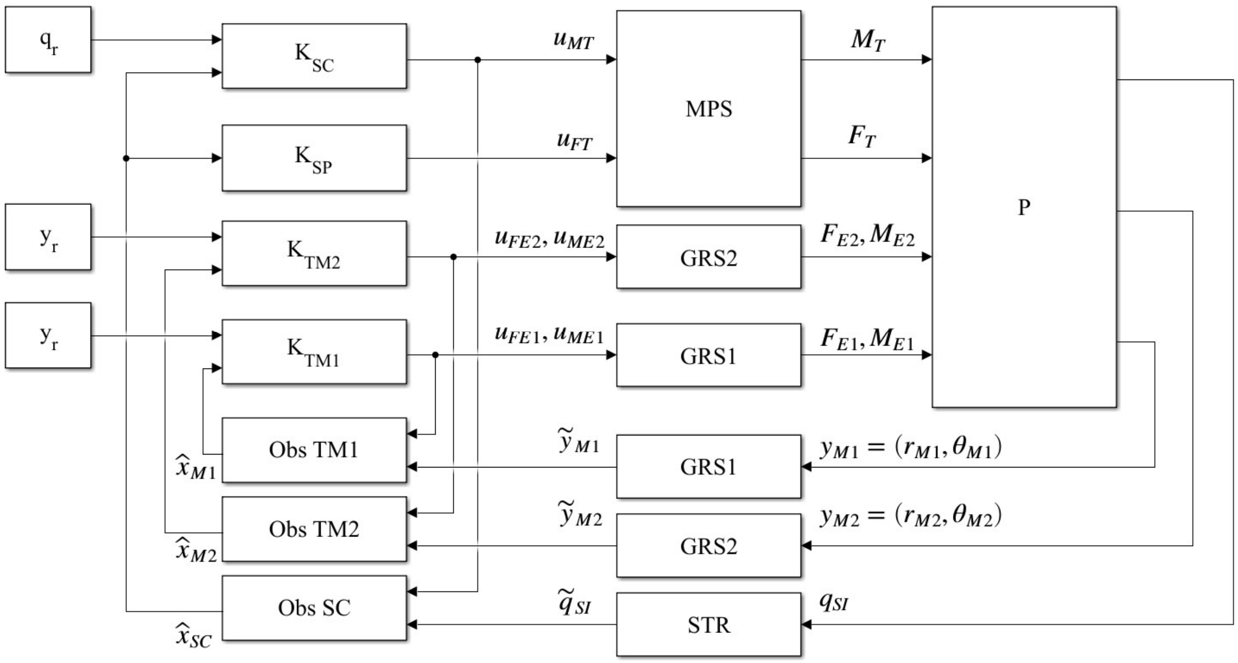

Figure 5 - Test Mass Release control architecture

3.4 Requirements Definition

The test mass release is a typical regulation problem, and the control performance can be evaluated by means of three figures of merit: overshoot, steady state error and settling time. The overshoot shall be lower than the GRS sensing range (2 mm). No specific requirements have to be set on the settling time, but in general it is a good practice to minimize the convergence time. In the MPC, this can be done by giving higher priority to the state error minimization in the cost function.

The definition of the requirement for the steady state error is less trivial. As discussed in section 3.1, the TM is affected by the stiffness disturbance, which depends on the test mass displacement relative to the cage centre and on the test mass attitude relative to the cage frame. This disturbance must be always lower than the actuation authority of the GRS. In Wide Range mode, the control authority is about 0.6 µN (z coordinate) and 9 nNm (yaw) which is sufficient to deal with the stiffness disturbance. However, when performing the transition to High Resolution mode, the control authority is reduced to 3.2 nN (z coordinate) and 0.015 nNm (yaw). This means that the residual displacement (steady state error of the position) at the end of the Wide Range Mode shall be sufficiently small to ensure stiffness disturbances that are lower than the actuation authority of the High Resolution mode. For instance, according to (1) and (2), the stiffness disturbance on the yaw coordinate is given by:

$$M_{sz} = +2.2 \cdot 10^{-6}\delta_x + 1.1 \cdot 10^{-6}\delta_y + 1.1 \cdot 10^{-6}\delta_z + 6 \cdot 10^{-8}\ \delta_\varphi + 6 \cdot 10^{-8}\delta_\theta + 1 \cdot 10^{-6}\delta_\psi.$$

By considering translation displacements $\delta_{x:z}$ of $2 \cdot 10^{-6}$ m and attitude displacements $\delta_{\varphi:\psi}$ of $5 \cdot 10^{-6}$ rad on the attitude coordinates, we obtain a stiffness disturbance torque M_{sz} that is almost equal to the saturation of the command input:

$$M_{sz} = 1.44 \cdot 10^{-11} \approx \bar{u}_\psi = 1.5 \cdot 10^{-1}\ \text{ Nm.}$$

Therefore, the steady state error of the TM position in Wide Range mode shall be within $\pm 2 \cdot 10^{-6}$ m, while the steady state error of the TM attitude in Wide Range mode shall be within $\pm 5 \cdot 10^{-6}$ rad, otherwise the stiffness disturbance becomes higher than the control authority when switching to High Resolution mode.

For what concerns the functional requirements, the control shall begin with a delay of 10 s after the test mass release, leaving enough time for the plungers' retraction [6]. Another functional requirement is related to the control frequency. The controller shall be discretized at 10 Hz, which is the operating frequency of the GRS.

3.5 Design

The discrete MPC optimization problem is formulated as follows:

$$\min J$$

$$J = \sum_{K=1}^{N} \left[S_y^{-1}(\boldsymbol{y}_k - \boldsymbol{y}_r)^T Q(\boldsymbol{y}_k - \boldsymbol{y}_r) + S_u^{-1}(\boldsymbol{u}_k)^T R(\boldsymbol{u}_k) + S_{ur}^{-1}(\boldsymbol{u}_k - \boldsymbol{u}_{k-1})^T R_{ur}(\boldsymbol{u}_k - \boldsymbol{u}_k) \right] \qquad (3)$$

subject to

$$\begin{aligned}\boldsymbol{x}_{k+1} &= A\boldsymbol{x}_k + B\boldsymbol{u}_k \\ \boldsymbol{y}_{\boldsymbol{k}} &= C\boldsymbol{x}_k + D\boldsymbol{u}_k\end{aligned} \tag{4}$$

$$-\boldsymbol{c}_{\boldsymbol{r}} \leq \boldsymbol{y}_k \leq \boldsymbol{c}_{\boldsymbol{r}} \tag{5}$$

$$-\bar{\boldsymbol{u}} \leq \boldsymbol{u}_k = \begin{bmatrix}\boldsymbol{F}_E \\ \boldsymbol{M}_E\end{bmatrix} \leq \bar{\boldsymbol{u}} \tag{6}$$

where k is the prediction step, N is the prediction horizon, $\boldsymbol{u}_k$ is the k-th input vector, $\boldsymbol{y}_k = (\boldsymbol{r}_{Mk} \quad \boldsymbol{\vartheta}_{Mk})$ is the k-th output vector, $\boldsymbol{y}_r = (\boldsymbol{r}_r \quad \boldsymbol{\vartheta}_r) = \boldsymbol{0} \ \ \forall\, k \geq 0$ is the reference vector. The cost function (3) minimizes the norm of the error between the predicted output and the reference, it minimizes the norm of the control input $\boldsymbol{u}_{\boldsymbol{k}}$ and its variation between two consecutive steps. Q, R, R_{ur} are diagonal weighting matrices, S_y^{-1}, S_u^{-1}, S_{ur}^{-1} are scaling factor matrices. As reported in Table 2, higher priority is given to the output error to minimize the convergence time, the scaling factor S_y^{-1} is chosen according to the order of magnitude of the TM release conditions, S_u^{-1} and S_{ur}^{-1} according to the GRS control authority. The internal state space model (4) is needed to predict the states up to the prediction horizon N and the outputs $\boldsymbol{y}_{\boldsymbol{k}}$ are used to compute the cost function. (4) is obtained by linearizing the nonlinear system [9] around the settling point $(\boldsymbol{r}_M \quad \boldsymbol{\vartheta}_M) = \boldsymbol{0}$ in absence of disturbances and with null TM stiffness coefficients. To perform predictions, the state space model (4) needs to be initialized with the last state estimate. Other constraints of the optimization problem are those on the test mass states (5) since it shall not leave the sensing ranges according to the values reported in the Appendix:

$$\boldsymbol{c}_{\boldsymbol{r}} = [2 \quad 2 \quad 2 \quad 100 \quad 100 \quad 100]^{\boldsymbol{T}} \cdot 10^{-3}.$$

Table 2. Cost function parameters

Q	R_u	R_{ur}	S_y^{-1}	S_u^{-1} , S_{ur}^{-1}
$\boldsymbol{I}_6$	$10^{-2}\boldsymbol{I}_6$	$10^{-1}\boldsymbol{I}_6$	$\begin{bmatrix}10^{-4}\boldsymbol{I}_3 & \boldsymbol{0}_3 \\ \boldsymbol{0}_3 & 10^{-2}\boldsymbol{I}_3\end{bmatrix}$	$\begin{bmatrix}10^{-6}\boldsymbol{I}_3 & \boldsymbol{0}_3 \\ \boldsymbol{0}_3 & 10^{-8}\boldsymbol{I}_3\end{bmatrix}$

Constraints (6) are the saturations on the control commands in WR mode:

$$\bar{\boldsymbol{u}} = [998 \quad 1056 \quad 595 \quad 11 \quad 16 \quad 9]^{\boldsymbol{T}} \cdot 10^{-9}.$$

The controller sampling time is set to $T_S = 0.10$ s (10Hz), which is the update rate of the electrostatic suspension. The prediction horizon N is set to 100 T_S to improve performance and the control horizon C is set to 1 T_S to have a faster algorithm.

For what concerns the spacecraft attitude control, a simple state feedback regulator with integral action is sufficient, since there are no particular constraints to be satisfied:

$$\mathfrak{q}_e = \hat{\mathfrak{q}}_{\boldsymbol{SI}}^{-1} \otimes \mathfrak{q}_{\boldsymbol{r}}$$

$$\boldsymbol{u}_{MT} = K_p \boldsymbol{q}_e - K_d \hat{\boldsymbol{\omega}}_{\boldsymbol{SI}} + K_I \frac{\boldsymbol{q}_e}{s}$$

where $\boldsymbol{q}_e$ is the vector part of $\mathfrak{q}_e$ and $\hat{\boldsymbol{\omega}}_{\boldsymbol{SI}}$ is the spacecraft estimated angular velocity. The parameter values ($K_p = 80,\ K_d = 160,\ K_I = 5$) have been chosen by means of a trial-and-error procedure, to ensure a small residual angular jitter at steady state.

The solar pressure acts on the spacecraft surface and provides a force that pushes the spacecraft towards the free-floating test masses and out of its nominal orbit. Therefore, it has to be properly compensated. The K_{SP} controller is a mathematical function which computes the solar pressure according to [16].

4. Results

A Monte Carlo test campaign was performed using a simulation environment which includes:

- Solar pressure noises (constant component and jitter).
- Constant disturbances and TM stiffness.
- Local environmental noises (force and torque noises acting on the test mass).
- Actuation and sensing noises of the electrostatic suspension as reported in the Appendix.

- MPS and Star tracker noise.

In the Monte Carlo simulations, the initial conditions were randomly chosen by means of a uniform distribution from the following variation range:

$$\left|\begin{matrix}\boldsymbol{r}_{M0}\\ \boldsymbol{\vartheta}_{M0}\end{matrix}\right| \leq \begin{bmatrix}455\ \mu\mathrm{m}\\ 16\ \mathrm{mrad}\end{bmatrix} \qquad \left|\begin{matrix}\dot{\boldsymbol{r}}_{M0}\\ \dot{\boldsymbol{\vartheta}}_{M0}\end{matrix}\right| \leq \begin{bmatrix}23\ \mu\mathrm{m/s}\\ 685\ \mu\mathrm{rad/s}\end{bmatrix}$$

where the previous values are the worse release conditions experienced by LISA Pathfinder [5].

Constant disturbances acting on the test mass were randomly initialized from the following variation range:

$$\left|\begin{matrix}\boldsymbol{F}_{DC}\\ \boldsymbol{M}_{DC}\end{matrix}\right| \leq 0.5\ \bar{\boldsymbol{u}}$$

more precisely, the boundaries were equal to the half of the saturations of the electrostatic suspension. The TM stiffness coefficients (1) were randomly chosen as follows:

$$-1.1K_S(i,j) \leq K_{st}(i,j) \leq 1.1K_S(i,j)$$

where K_s is equal to (2).

Once the test mass is released and captured electrostatically, the constellation acquisition phase begins. Once it has been accomplished and the laser links have been acquired, the system enters drag free mode. However, before doing so, the GRS has to switch from Wide Range to High Resolution mode, while the SC attitude sensor shall switch from the star trackers to the DWS. This switch determines a reduction of the GRS command input saturations and a reduction of the actuation and sensing noises according to the values reported in the Appendix. To the test control system behavior during the transition from Wide Range to High Resolution mode and from the star trackers to the DWS, an arbitrary operating mode switch was included in each simulation at 1000 s. The Monte Carlo results are reported in Fig. 6 with a simulation horizon of 1500 s, to check the response when switching to HR mode at 1000 s. 500 simulations were performed and a success rate of 100% was obtained. The maximum settling time was about 200 s on the x-y translations and 400 s on the vertical translation. This is due to the lower actuation authority along the z coordinate as shown in Fig. 7. The attitude coordinates converged within 200 s (roll and yaw), 150 s (pitch).

The worse overshoot was about 1.4 mm on the test mass vertical translation. This means that no simulation violated constraint (5) about the GRS measurement range. In Fig. 7, it can be noted that the force components do not violate constraint (6) about the command saturations. Moreover, at the beginning of the simulation, the test mass is quickly escaping from the cage centre due to the bad initial conditions. Consequently, the MPC applies the maximum forces to minimize the output error. Once the test mass is close to the reference, the term related to the output error in the cost function (3) tends to zero, and therefore the MPC starts to minimize the command input. Fig. 8 shows the steady state errors in Wide Range mode, which are roughly within ±2 μm for the translation coordinates, ±4 μrad for the attitude coordinates. When switching to High Resolution mode, no stability issues occurred, and further improvements were obtained in terms of noise amplitude. The same holds for the command inputs. The obtained results are summarized in Tables 3 and 4.

One last comment is related to the spacecraft attitude control. While the test masses are released and controlled, the spacecraft has to keep the reference attitude compensating for the solar pressure torque and the internal reaction forces/torques of the two electrostatic suspensions.

Fig. 9 shows that the SC attitude error has a zero average, but in the first 1000 s it is quite noisy because of the star trackers and despite the presence of a Kalman filter. When switching to DWS (available only after the laser links of the constellation have been acquired) the sensing noise is greatly reduced, as well as the residual jitter of the attitude error, of about 2 orders of magnitude.

Table 3. Output performance

Output Variable	Max Settling Time	Max Overshoot	Steady State Error Range (WR)	Steady State Error Range (HR)
x	200 s	$1.1 \cdot 10^{-3}$ m	$\pm 1.5 \cdot 10^{-6}$ m	$\pm 4 \cdot 10^{-7}$ m
y	200 s	$1.1 \cdot 10^{-3}$ m	$\pm 3 \cdot 10^{-6}$ m	$\pm 4 \cdot 10^{-7}$ m
z	400 s	$1.4 \cdot 10^{-3}$ m	$\pm 2 \cdot 10^{-6}$ m	$\pm 3 \cdot 10^{-7}$ m
ϑ_x	200 s	$2.1 \cdot 10^{-2}$ rad	$\pm 4 \cdot 10^{-6}$ rad	$\pm 1 \cdot 10^{-6}$ rad
ϑ_y	150 s	$1.7 \cdot 10^{-2}$ rad	$\pm 4 \cdot 10^{-6}$ rad	$\pm 1.5 \cdot 10^{-6}$ rad
ϑ_z	200 s	$2.5 \cdot 10^{-2}$ rad	$\pm 4 \cdot 10^{-6}$ rad	$\pm 0.8 \cdot 10^{-6}$ rad

Table 4. Command activity (peak to peak values)

Command Input	TM capture	WR steady state	HR steady state
F_X	±998 nN	±50 nN	±4 nN
F_y	±1056 nN	±70 nN	±4 nN
F_z	±595 nN	±60 nN	±2 nN
M_X	±11 nNm	±1.5 nNm	±0.1 nN
M_y	±16 nNm	±3 nNm	±0.2 nN
M_z	±9 nNm	±3 nNm	±0.2 nN

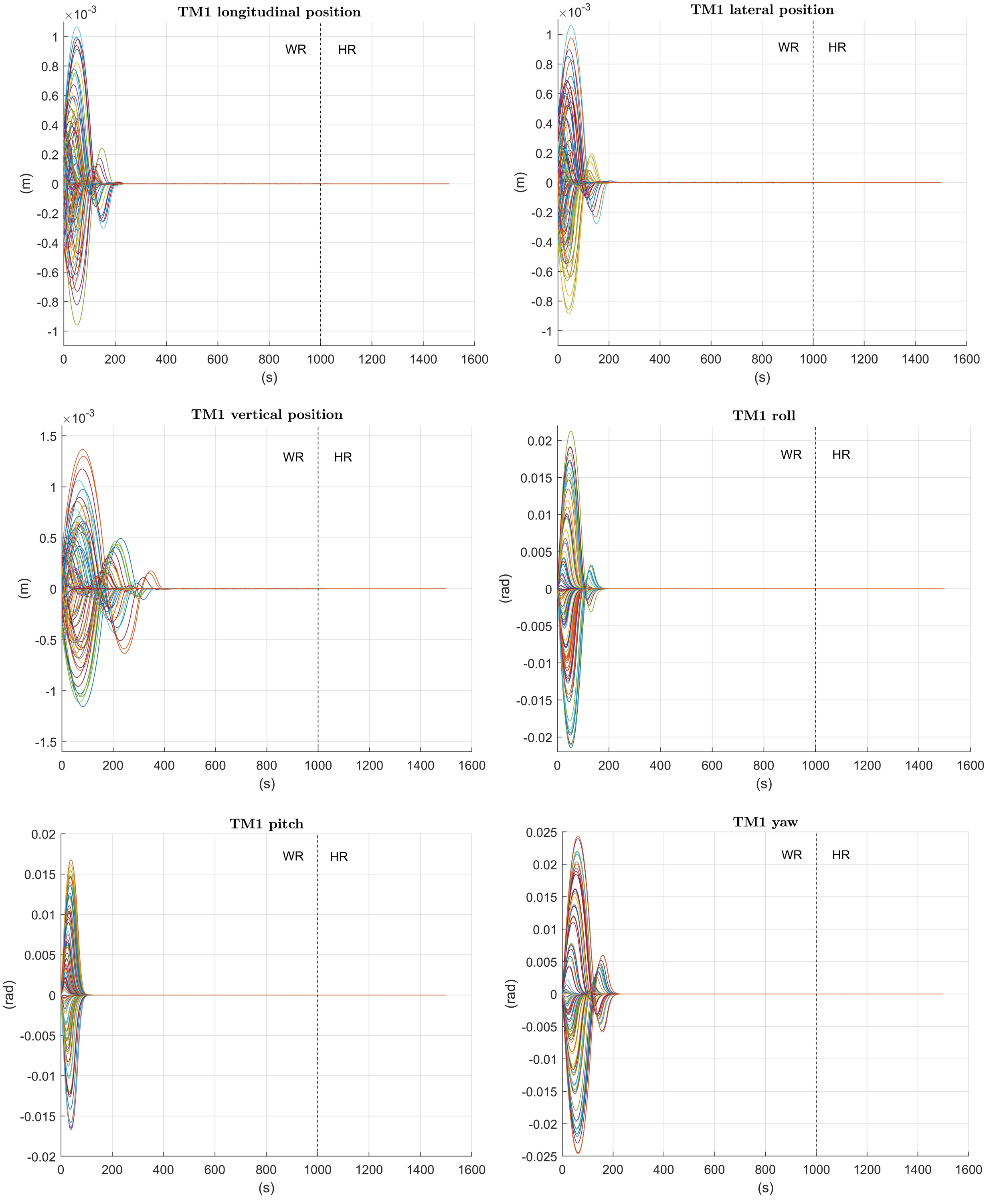

TM1 longitudinal position

TM1 lateral position

TM1 vertical position

TM1 roll

TM1 pitch

TM1 yaw

Figure 6 – TM position and attitude w.r.t. cage frame

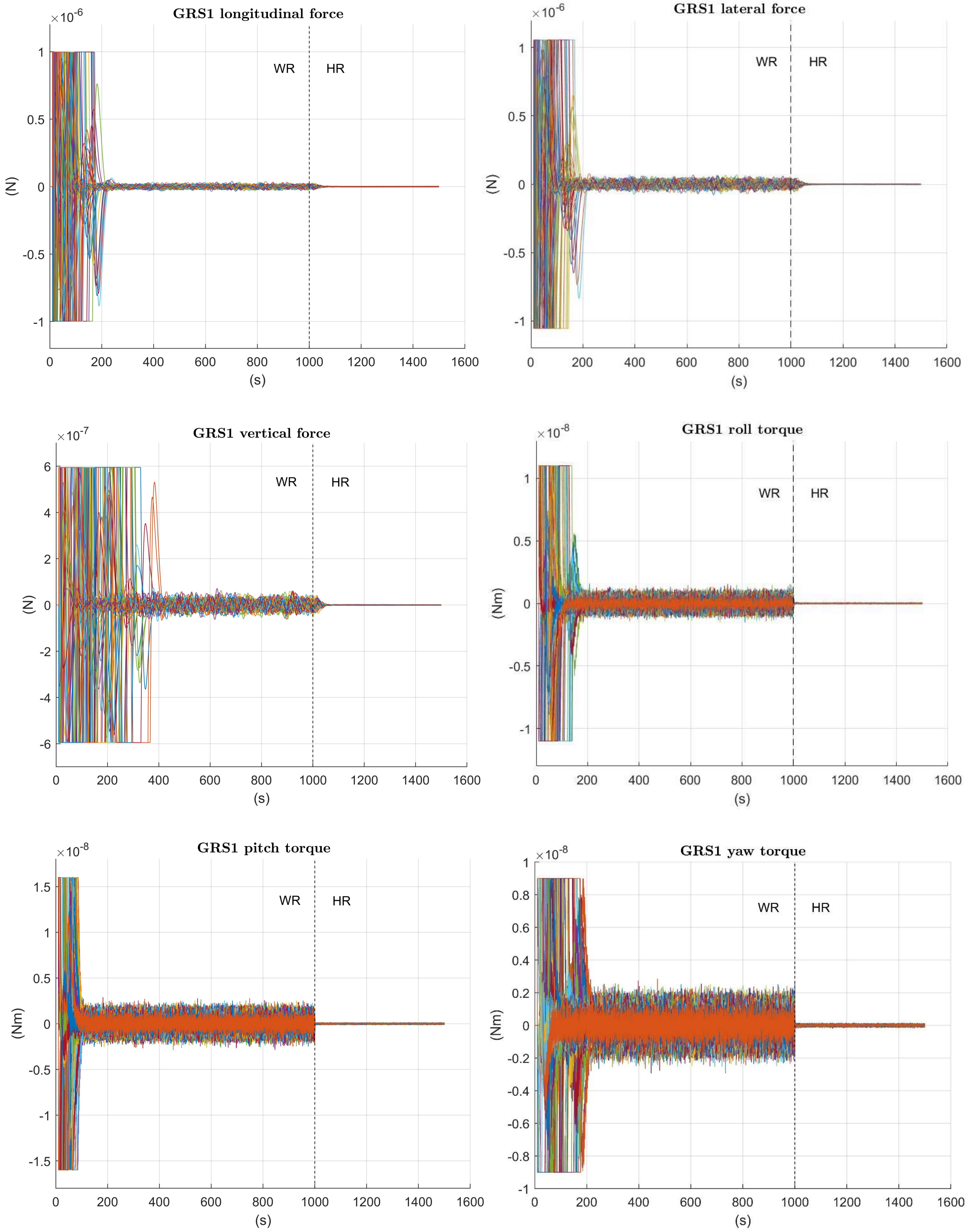

Figure 7 – GRS force and torque components

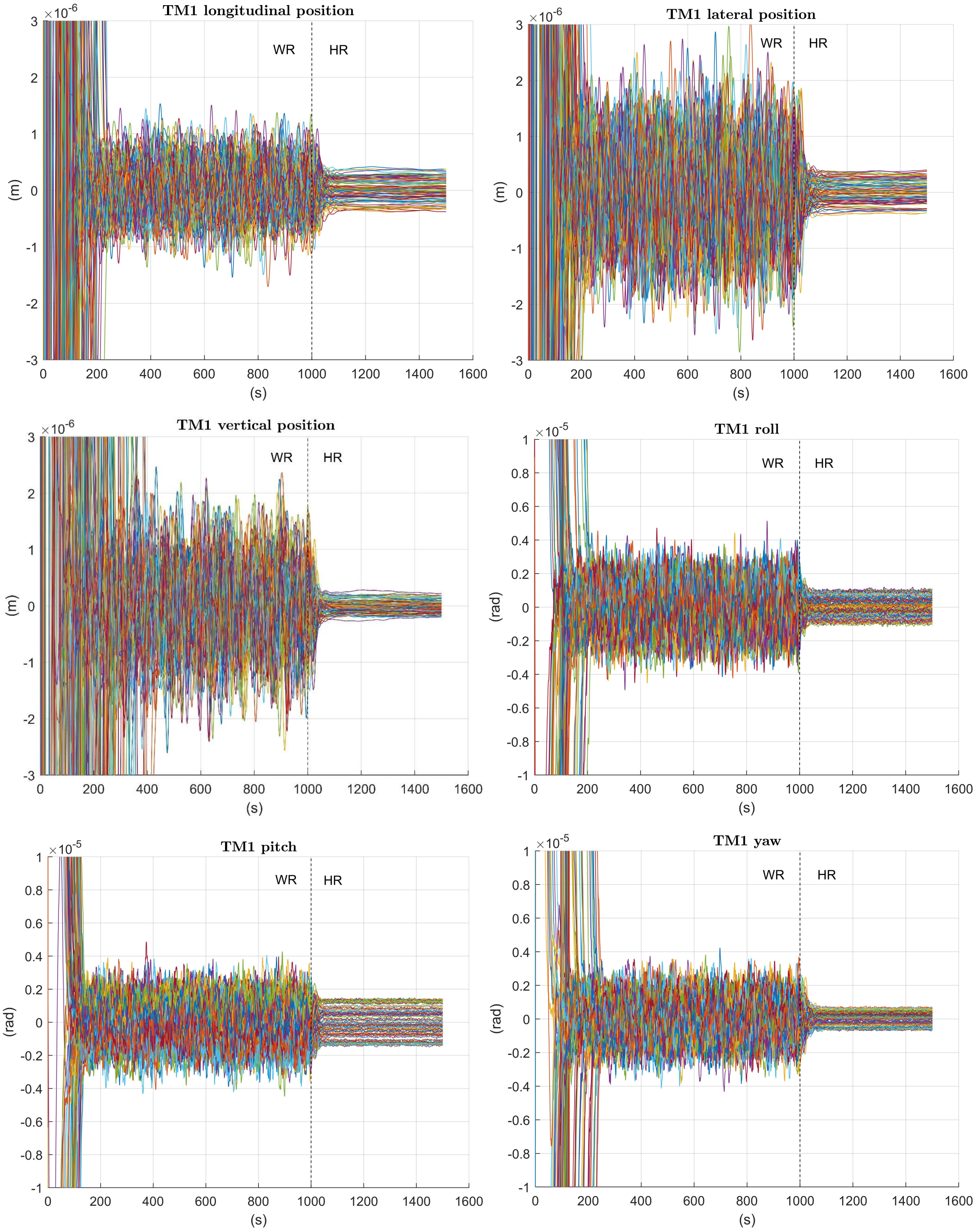

Figure 8 – Steady state and transition to High Resolution mode

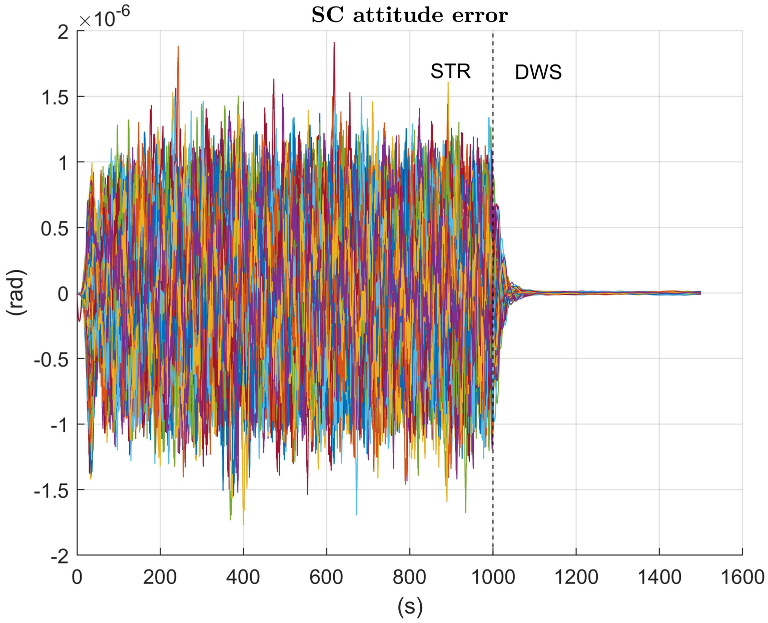

Figure 9 – SC attitude error

5. Conclusions

The test mass release control problem of the LISA mission has been considered in this paper. The plunger retraction of the locking mechanism provides to the test mass poor initial condition, as experienced in-flight by LISA Pathfinder. Together with the low actuation authority and the TM stiffness disturbances, this makes the electrostatic capture a difficult task.

The control architecture proposed in this work consisted in two different MPC controllers, one for each electrostatic suspension, that control in parallel the two test-masses. The spacecraft attitude is controlled by means of a state feedback regulator, while the solar radiation pressure force is compensated in open loop, to avoid that spacecraft translates relative to the mass while the latter is being released and captured. The two MPCs have been designed considering a quadratic cost function based on the output error, the input amplitude and the input rate. For what concerns the constraints, the command saturations of the GRS in Wide Range and High Resolution mode have been considered, together with some spatial bounds on the test-mass position and attitude. The

MPC controllers and the SC attitude state-feedback regulator have been tested in a Monte Carlo test campaign. In terms of stability, a success rate of 100% was obtained in 300 simulations. For what concerns the performance, it was obtained a worst-case settling time of 200 s on the x-y translations and about 400 s on the z translation. The attitude coordinates converged within 200 s (roll and yaw) and 150 s (pitch). In Wide Range mode, the position steady state errors were respectively within ±2 µm, while the attitude steady state errors were within ±4 µrad. The transition from Wide Range to High Resolution did not caused stability problems and allowed to reduce the amplitude of the residual jitter.

Given the results of the present study, Model Predictive Control proved to be an effective control technique for this application. Together with the sliding mode already tested in-flight by LISA Pathfinder, it can be considered for future developments of the LISA space mission.

Acknowledgements

This work was funded by the European Space Agency. The Authors ensure complete objectivity in the data interpretation and writing of the paper. The view expressed in this work cannot be taken as the official position of the European Space Agency.

Appendix

Table A1 reports the GRS command saturations and the noise filters to be applied in cascade to a white noise generator.

Table A1 – GRS actuation features

	DoF	Wide Range Mode	High Resolution Mode
Force saturation	x	998 nN	5.4 nN
	y	1056 nN	5.7 nN
	z	595 nN	3.2 nN
Torque saturation	X	11 nNm	0.02 nNm
	Y	16 nNm	0.03 nNm
	Z	9 nNm	0.015 nNm
Force noise	n_x	$6 \cdot 10^{-15} \frac{(s + 1.257 \cdot 10^{-4})^2}{(s + 5.13 \cdot 10^{-6})^2} \frac{\mathrm{N}}{\sqrt{\mathrm{Hz}}}$	$6 \cdot 10^{-16} \frac{(s + 1.257 \cdot 10^{-4})^2}{(s + 5.13 \cdot 10^{-6})^2} \frac{\mathrm{N}}{\sqrt{\mathrm{Hz}}}$
	n_y	$5 \cdot 10^{-14} \frac{(s + 1.257 \cdot 10^{-4})^2}{(s + 2.81 \cdot 10^{-6})^2} \frac{\mathrm{N}}{\sqrt{\mathrm{Hz}}}$	$5 \cdot 10^{-15} \frac{(s + 1.257 \cdot 10^{-4})^2}{(s + 2.81 \cdot 10^{-6})^2} \frac{\mathrm{N}}{\sqrt{\mathrm{Hz}}}$
	n_z	$5 \cdot 10^{-14} \frac{(s + 1.257 \cdot 10^{-4})^2}{(s + 2.81 \cdot 10^{-6})^2} \frac{\mathrm{N}}{\sqrt{\mathrm{Hz}}}$	$5 \cdot 10^{-15} \frac{(s + 1.257 \cdot 10^{-4})^2}{(s + 2.81 \cdot 10^{-6})^2} \frac{\mathrm{N}}{\sqrt{\mathrm{Hz}}}$
Torque noise	n_X	$5 \cdot 10^{-16} \frac{(s + 1.257 \cdot 10^{-4})^2}{(s + 2.81 \cdot 10^{-6})^2} \frac{\mathrm{Nm}}{\sqrt{\mathrm{Hz}}}$	$5 \cdot 10^{-17} \frac{(s + 1.257 \cdot 10^{-4})^2}{(s + 2.81 \cdot 10^{-6})^2} \frac{\mathrm{Nm}}{\sqrt{\mathrm{Hz}}}$
	n_Y	$5 \cdot 10^{-16} \frac{(s + 1.257 \cdot 10^{-4})^2}{(s + 2.81 \cdot 10^{-6})^2} \frac{\mathrm{Nm}}{\sqrt{\mathrm{Hz}}}$	$5 \cdot 10^{-17} \frac{(s + 1.257 \cdot 10^{-4})^2}{(s + 2.81 \cdot 10^{-6})^2} \frac{\mathrm{Nm}}{\sqrt{\mathrm{Hz}}}$
	n_Z	$5 \cdot 10^{-16} \frac{(s + 1.257 \cdot 10^{-4})^2}{(s + 2.81 \cdot 10^{-6})^2} \frac{\mathrm{Nm}}{\sqrt{\mathrm{Hz}}}$	$5 \cdot 10^{-17} \frac{(s + 1.257 \cdot 10^{-4})^2}{(s + 2.81 \cdot 10^{-6})^2} \frac{\mathrm{Nm}}{\sqrt{\mathrm{Hz}}}$

Table A2 reports the GRS sensing ranges and measurements noises in form of filters to be applied in cascade to a white noise generator.

Table A2 – GRS sensing features

	DoF	Wide Range Mode	High Resolution Mode
Position range	x	2 mm	100 μm
	y	2 mm	100 μm
	z	2 mm	150 μm
Attitude range	X	100 mrad	9 mrad
	Y	100 mrad	5 mrad
	Z	100 mrad	9 mrad

Table A3 – GRS measurement noises (Wide Range Mode)

Position Sensing Noise	x	$2.5 \cdot 10^{-8} \frac{(s+3 \cdot 10^{-2})(s+5.4 \cdot 10^{-3})(s+9.6 \cdot 10^{-4})(s+1.7 \cdot 10^{-4})}{(s+2.58 \cdot 10^{-2})(s+2.933 \cdot 10^{-3})(s+4.333 \cdot 10^{-4})(s+6 \cdot 10^{-5})} \frac{\mathrm{m}}{\sqrt{\mathrm{Hz}}}$
	y	$2.5 \cdot 10^{-8} \frac{(s+3 \cdot 10^{-2})(s+5.4 \cdot 10^{-3})(s+9.6 \cdot 10^{-4})(s+1.7 \cdot 10^{-4})}{(s+2.58 \cdot 10^{-2})(s+2.933 \cdot 10^{-3})(s+4.333 \cdot 10^{-4})(s+6 \cdot 10^{-5})} \frac{\mathrm{m}}{\sqrt{\mathrm{Hz}}}$
	z	$4 \cdot 10^{-8} \frac{(s+3 \cdot 10^{-2})(s+5.4 \cdot 10^{-3})(s+9.6 \cdot 10^{-4})(s+1.7 \cdot 10^{-4})}{(s+2.58 \cdot 10^{-2})(s+2.933 \cdot 10^{-3})(s+4.333 \cdot 10^{-4})(s+6 \cdot 10^{-5})} \frac{\mathrm{m}}{\sqrt{\mathrm{Hz}}}$
Attitude sensing noise	X	$3 \cdot 10^{-6} \frac{(s+3 \cdot 10^{-2})(s+5.4 \cdot 10^{-3})(s+9.6 \cdot 10^{-4})(s+1.7 \cdot 10^{-4})}{(s+2.58 \cdot 10^{-2})(s+2.933 \cdot 10^{-3})(s+4.333 \cdot 10^{-4})(s+6 \cdot 10^{-5})} \frac{\mathrm{rad}}{\sqrt{\mathrm{Hz}}}$
	Y	$1.8 \cdot 10^{-6} \frac{(s+3 \cdot 10^{-2})(s+5.4 \cdot 10^{-3})(s+9.6 \cdot 10^{-4})(s+1.7 \cdot 10^{-4})}{(s+2.58 \cdot 10^{-2})(s+2.933 \cdot 10^{-3})(s+4.333 \cdot 10^{-4})(s+\cdot 10e^{-5})} \frac{\mathrm{rad}}{\sqrt{\mathrm{Hz}}}$
	Z	$1.8 \cdot 10^{-6} \frac{(s+3 \cdot 10^{-2})(s+5.4 \cdot 10^{-3})(s+9.6 \cdot 10^{-4})(s+1.7 \cdot 10^{-4})}{(s+2.58 \cdot 10^{-2})(s+2.933 \cdot 10^{-3})(s+4.333 \cdot 10^{-4})(s+\cdot 10e^{-5})} \frac{\mathrm{rad}}{\sqrt{\mathrm{Hz}}}$

Table A4 – GRS measurement noises (High Resolution Mode)

Position Sensing Noise	x	$1.8\cdot10^{-9}\frac{(s+3\cdot10^{-2})(s+5.4\cdot10^{-3})(s+9.6\cdot10^{-4})(s+1.7\cdot10^{-4})}{(s+2.58\cdot10^{-2})(s+2.933\cdot10^{-3})(s+4.333\cdot10^{-4})(s+6\cdot10^{-5})}\frac{\mathrm{m}}{\sqrt{\mathrm{Hz}}}$
	y	$1.8\cdot10^{-9}\frac{(s+3\cdot10^{-2})(s+5.4\cdot10^{-3})(s+9.6\cdot10^{-4})(s+1.7\cdot10^{-4})}{(s+2.58\cdot10^{-2})(s+2.933\cdot10^{-3})(s+4.333\cdot10^{-4})(s+6\cdot10^{-5})}\frac{\mathrm{m}}{\sqrt{\mathrm{Hz}}}$
	z	$3e^{-9}\frac{(s+3\cdot10^{-2})(s+5.4\cdot10^{-3})(s+9.6\cdot10^{-4})(s+1.7\cdot10^{-4})}{(s+2.58\cdot10^{-2})(s+2.933\cdot10^{-3})(s+4.333\cdot10^{-4})(s+6\cdot10^{-5})}\frac{\mathrm{m}}{\sqrt{\mathrm{Hz}}}$
Attitude sensing noise	X	$2e^{-7}\frac{(s+3\cdot10^{-2})(s+5.4\cdot10^{-3})(s+9.6\cdot10^{-4})(s+1.7\cdot10^{-4})}{(s+2.58\cdot10^{-2})(s+2.933\cdot10^{-3})(s+4.333\cdot10^{-4})(s+6\cdot10^{-5})}\frac{\mathrm{rad}}{\sqrt{\mathrm{Hz}}}$
	Y	$1.2\cdot10^{-7}\frac{(s+3\cdot10^{-2})(s+5.4\cdot10^{-3})(s+9.6\cdot10^{-4})(s+1.7\cdot10^{-4})}{(s+2.58\cdot10^{-2})(s+2.933\cdot10^{-3})(s+4.333\cdot10^{-4})(s+6\cdot10^{-5})}\frac{\mathrm{rad}}{\sqrt{\mathrm{Hz}}}$
	Z	$1.2\cdot10^{-7}\frac{(s+3\cdot10^{-2})(s+5.4\cdot10^{-3})(s+9.6\cdot10^{-4})(s+1.7\cdot10^{-4})}{(s+2.58\cdot10^{-2})(s+2.933\cdot10^{-3})(s+4.333\cdot10^{-4})(s+6\cdot10^{-5})}\frac{\mathrm{rad}}{\sqrt{\mathrm{Hz}}}$

Table A5 – Star tracker and DWS measurement noises

Star tracker	x	White noise with st.d. $\sigma_x = 4.85\cdot10^{-6}$ rad
	y	White noise with st.d. $\sigma_y = 4.85\cdot10^{-6}$ rad
	z	White noise with st.d. $\sigma_z = 4.85\cdot10^{-5}$ rad
DWS	X	$\frac{1}{300}35e^{-9}\frac{(s+6\cdot10^{-3})^2}{(s+6\cdot10^{-5})^2}\frac{\mathrm{rad}}{\sqrt{\mathrm{Hz}}}$
	Y	$\frac{1}{300}35e^{-9}\frac{(s+6\cdot10^{-3})^2}{(s+6\cdot10^{-5})^2}\frac{\mathrm{rad}}{\sqrt{\mathrm{Hz}}}$
	Z	$\frac{1}{300}35e^{-9}\frac{(s+6\cdot10^{-3})^2}{(s+6\cdot10^{-5})^2}\frac{\mathrm{rad}}{\sqrt{\mathrm{Hz}}}$

References

[1] P. Amaro-Seoane et al., Laser Interferometer Space Antenna, arXiv e-prints, p. arXiv:1702.00786, Feb 2017.

[2] M. Sallusti et al., LISA system design highlights, Class. Quantum Grav. **26** 094015, 2009.

[3] ESA, LISA Yellow Book, Assessment Study Report, 2011.

[4] C Zanoni et al., Summary of the results of the LISA-Pathfinder Test Mass release, Journal of Physics: Conference Series. 610 012022, 2015.

[5] D. Bortoluzzi et al., Injection of a Body into a Geodesic: Lessons Learnt from the LISA Pathfinder Case, Nasa.gov, 20160008114, 2016.

[6] A. Schleicher et al., In-Orbit Performance of the LISA Pathfinder Drag Free and Attitude Control System, 10th International ESA GNC Conference, 2017.

[7] M. Mirshams et al., Station keeping and momentum management of low-thrust satellites using MPC, Aerospace Science and Technology, Volume 48, January 2016, p. 140-145.

[8] A. Golzari, et al., Quaternion based linear time-varying model predictive attitude control for satellites with two reaction wheels, Aerospace Science and Technology, Volume 98, March 2020.

[9] Q. Hu et al., Trajectory optimization for accompanying satellite obstacle avoidance, Aerospace Science and Technology, Volumes 82–83, November 2018.

[10] Q. Li et al., Model predictive control for autonomous rendezvous and docking with a tumbling target, Aerospace Science and Technology, Volume 69, October 2017.

[11] F. Montemurro et al., Control Design of the Test Mass Release Mode for the LISA Pathfinder Mission, AIP Conference Proceedings 873 583, 2006.

[12] F. Montemurro et al., Sliding Mode Technique Applied to the Test Mass Suspension Control, IFAC Proceedings Volumes, Volume 40, Issue 7, pp. 627-632, 2007.

[13] S. Vidano et al., The LISA DFACS: Preliminary Model Predictive Control for the Test Mass Release Phase, 71st International Astronautical Congress, IAC-20,C1,9,5,x58065, 2020.

[14] E. Camacho and C. Bordons Alba, Model Predictive Control, Springer, 2007.

[15] S. Vidano et al., The LISA DFACS: a Nonlinear Model for the Spacecraft Dynamics, Aerospace Science and Technology, 2020. (accepted with minor review)

[16] O. Jennrich, LISA Technology and Instrumentation, Classical and Quantum Gravity, 2009. doi 10.1088/0264-9381/26/15/153001.

[17] D. Bortoluzzi et al. On-ground testing of the role of adhesion in the LISA-Pathfinder test mass injection phase, Advances in Space Research 59, 2017.

[18] D. Gerardi, Advanced drag-free concepts for future space-based interferometers: acceleration noise performance, Review of Scientific Instruments 85, 011301, 2014.

[19] S. Merkowitz, Self-Gravity modelling for LISA, Classical and Quantum Gravity 22, pp.395-402, 2005.

[20] T. Ziegler, Test Mass Stiffness Estimation for the LISA Pathfinder Drag-Free System, AIAA GNC Conference and Exhibits, 2007.

[21] R. M. Georgevic, Mathematical Model of the Solar Radiation Force and Torques Acting on the Components of a Spacecraft, NASA JPL, 1971